3D nanoscale analysis of bone healing around degrading Mg implants evaluated by X-ray scattering tensor tomography

Acta Biomaterialia xxx (xxxx) xxx

Contents lists available at ScienceDirect

Acta Biomaterialia

journal homepage: www.elsevier.com/locate/actbio

Full length article

3D nanoscale analysis of bone healing around degrading Mg implants evaluated by X-ray scattering tensor tomography

Marianne Liebi[a,b,c,*], Viviane Lutz-Bueno[b,1], Manuel Guizar-Sicairos[b], Bernd M. Schönbauer[d], Johannes Eichler[e], Elisabeth Martinelli[e], Jörg F. Löffler[f], Annelie Weinberg[e], Helga Lichtenegger[d], Tilman A. Grünewald[g,2,*]

[a] Department of Physics, Chalmers University of Technology, 41296 Gothenburg, Sweden
[b] Paul Scherrer Institut, 5232 Villigen PSI, Switzerland
[c] Center for X-ray Analytics, Swiss Federal Laboratories for Materials Science and Technology (Empa), 9014 St. Gallen, Switzerland
[d] Institute of Physics and Materials Science, University of Natural Resources and Life Science (BOKU), 1190 Vienna, Austria
[e] Department of Orthopaedics, Medical University Graz, 8010 Graz, Austria
[f] Laboratory of Metal Physics and Technology, Department of Materials, ETH Zurich, 8093 Zurich, Switzerland
[g] European Synchrotron Radiation Facility (ESRF), 38000 Grenoble, France

ARTICLE INFO

Article history:
Received 13 January 2021
Revised 1 July 2021
Accepted 23 July 2021
Available online xxx

Keywords:
Biomineralization
Implant degradation
X-ray scattering
Tomography
Degradable magnesium implants

ABSTRACT

The nanostructural adaptation of bone is crucial for its biocompatibility with orthopedic implants. The bone nanostructure also determines its mechanical properties and performance. However, the bone's temporal and spatial nanoadaptation around degrading implants remains largely unknown. Here, we present insights into this important bone adaptation by applying scanning electron microscopy, elemental analysis, and small-angle X-ray scattering tensor tomography (SASTT). We extend the novel SASTT reconstruction method and provide a 3D scattering reciprocal space map per voxel of the sample's volume. From this reconstruction, parameters such as the thickness of the bone mineral particles are quantified, which provide additional information on nanostructural adaptation of bone during healing. We selected a rat femoral bone and a degrading ZX10 magnesium implant as model system, and investigated it over the course of 18 months, using a sham as control. We observe that the bone's nanostructural adaptation starts with an initially fast interfacial bone growth close to the implant, which spreads by a re-orientation of the nanostructure in the bone volume around the implant, and is consolidated in the later degradation stages. These observations reveal the complex bulk bone-implant interactions and enable future research on the related biomechanical bone responses.

Statement of significance

Traumatic bone injuries are among the most frequent causes of surgical treatment, and often require the placement of an implant. The ideal implant supports and induces bone formation, while being mechanically and chemically adapted to the bone structure, ensuring a gradual load transfer. While magnesium implants fulfill these requirements, the nanostructural changes during bone healing and implant degradation remain not completely elucidated. Here, we unveil these processes in rat femoral bones with ZX10 magnesium implants and show different stages of bone healing in such a model system.

1. Introduction

Bone has a complex structure that self-organizes over nine orders of magnitude. These orders start from the fractal organization of the hydroxyapatite (HAP) mineral particles on the nanometer scale [1] and expand towards the macroscopic bone shape. Long bones, such as a femur, possess three major constituents: trabec-

E-mail addresses: marianne.liebi@chalmers.se (M. Liebi), tilman.grunewald@fresnel.fr (T.A. Grünewald).
[1] Current address: Laboratory of Food and Soft Materials, Department of Health Sciences and Technology, ETH Zurich, 8093 Zurich, Switzerland
[2] Current address: Aix-Marseille Univ, CNRS, Centrale Marseille, Institut Fresnel, 13013 Marseille, France
* Corresponding authors.

https://doi.org/10.1016/j.actbio.2021.07.060
1742-7061/

ular bone, cortical bone and the bone marrow. Each constituent shows a rich functional structure on the micro- and macroscale, and different organizational motifs from the meso- to nanoscale [2]. Despite ongoing discussions about the bone's nanostructural organization, it is generally agreed that its nano-structured building blocks are composed of collagen fibrils, extrafibrillar matrix proteins and HAP mineral particles. In the classical model [3], the collagen fibers are mineralized in the gap zones of the overlapping collagen molecules. The mineral particles inside a single collagen fiber are thought to be layered with respect to each other [4], where this layered register even extends over several fibrils (~500 nm) in the case of mineralized turkey leg tendon [5]. Over larger lengths scales of a few micrometers, the individual layers are thought to be rotated around the collagen fiber axis, while retaining their preferred orientation along this axis [6].

The engineering of orthopedic implants and their application underwent transformational development in recent years. Bioinert, bio-compatible, and bio-active materials have improved the adaptation of the implants in the body. Degrading implants attracted considerable interest in recent years, where different material classes, such as metals [7], polymers [8], or ceramics [9], with different specific strengths have been investigated. Biodegradable metallic implants feature excellent mechanical properties and the Young's modulus of Mg-based implants matches very well that of bone, which reduces stress shielding. Mg has also been reported to enhance bone formation [10,11]. Furthermore, without the need of implant removal, scars, trauma and costs from a second surgery can be avoided.

Potential clinical applications of degrading Mg implants are in oral or craniofacial surgery as well as in orthopedic surgery and traumatology. In pediatric orthopedics, implant degradation may circumvent the imperative surgical implant removal due to the still growing young skeleton. This would not only reduce costs and stress for the young patients, but also reduce the risk of damage to the still active growth plate and of infection due to the second surgical intervention. In the field of oral and craniofacial surgery, bioresorbable materials may promote periodontal tissue or bone regeneration without the need of removing the implant. Mg and its alloys may also be used as pure synthetic bone regenerative materials and in osteosynthetic indication. Recently, a preclinical study with miniature pigs was also performed, with the aim of developing plates and screws for zygomatic and orbital fracture reduction [12].

While biodegradable implants have improved the compatibility between implant and body, the impact on the nanostructural bone adaptation during the healing process and implant degradation remains not fully elucidated. However, detailed investigation of the bone's nano-structural adaptation during implant degradation and the corresponding implant-bone interactions at the interface are of great interest in the medical and biomaterial communities. The direct interface (~20 µm) is characterized by a degradation layer that formed by an electrochemical reaction between the implant and the surrounding physiological medium [13]. This layer is composed of $Mg(OH)_2$ as the primary reduction product and Ca phosphates that formed in the later stages [10,14].

Only recently started research to focus on the nanostructural adaptation of bone triggered by implant placement [15]. Besides classical techniques such as histology, computed tomography, and electron-based methods to investigate the bone structure, small-angle X-ray scattering (SAXS) has become key to uncover the bone nanostructure and its adaptation. Fratzl and coworkers [16] contributed pioneering work on the nanostructural arrangement of mineral particles in bone and the analytical treatment of SAXS data [17]. The bone-implant interactions have since then become a widely investigated research area. Noteworthy publications on non-degrading implants include the work of Bünger et al. [18], which showed that mineral platelets have orientational rearrangement around a non-degrading titanium (Ti) screw implant. Hoerth et al. [19] revealed the bone-growth process around zirconium (Zr) and Ti implants. A recent study [20] using scanning wide- and small-angle scattering (WAXS/SAXS) reported no significant difference in the degree of orientation, orientation divergence or mineral particle thickness in bone around two different biodegradable magnesium–gadolinium (Mg–Gd) alloys, polyether ether ketone (PEEK) and Ti implants, respectively. They did, however, report a difference in (310) lattice spacing and crystallite size between titanium and Mg–Gd alloys, which indicates a possible deposition of Mg in the degradation layer.

We showed significant alterations in the bone nanostructure within 20 µm from the bone-implant interface by microbeam scanning diffraction [21]. The interface is characterized by high Mg levels, a smaller mineral particle size and a contracted HAP mineral structure compared to the bulk of the bone. These changes were interpreted as bone growth and the inclusion of Mg into the HAP lattice. Recent work has also illustrated the adaptation of bone nanostructure as a response to the degrading implants. Two findings were particularly striking: (i) the early onset of nanostructural reorientation (after 1 month), which, however, showed no evident changes in the mineral particle size and (ii) the late onset of bone growth after 12 months and persistent orientation effects after 18 months. These findings were corroborated by mechanical studies that confirmed the slow healing rates, based on the lowered hardness and stiffness of the bone in the vicinity of the degrading implants, which normalized after complete bone healing [22]. The main conclusion of that work was that Mg implants induce a localized adaptation of the nanostructure, which needs to be considered in the design of degrading metallic implants. Nevertheless, it should be noted that this study was performed in 2D, and it was limited to scanning the sample in the implant cross-sectional plane, making it impossible to detect more intricate orientation patterns, such as a wrapping around the implant.

This limitation is generic to scanning techniques and is especially problematic when the structural adaptations are expected to be volumetric, such as with degrading implants. 3D diffraction tomography already revealed promising insights into the nanostructural characterization of biominerals [23]. The extension of scanning scattering techniques from 2D to 3D has posed a difficult challenge and was recently solved for oriented nanostructures with a tensor tomography approach by Liebi et al. and Schaff et al. [24,25]. This development enables the study of bone nanostructure and the direct comparison of orientational motifs in bone [26], and thus the investigation of nanostructural adaptation of the entire bone-implant interactions in 3D.

Focusing on implant materials in clinical application, the rare-earth containing alloy WE43 (Mg-3.56% yttrium (Y)-2.20% neodymium (Nd)-0.47% zirconium (Zr), in wt%) has found clinical application in the form of screws for the fixation of osteochondral fragments [27] (MAGNEZIX®, Synthelix AG, Hannover, Germany), and an alternative for internal fixation of hand fractures is based on a Mg–Ca–Zn alloy (Resomet™, U & I Corp, Seoul, Korea) [10]. A recent overview of clinical applications was presented by Han et al. [7]. The implant material ZX10 used in this study is a lean Mg–Zn–Ca alloy, with a composition of Mg-1.0% zinc (Zn)-0.3% calcium (Ca) (in wt%) [28]. ZX10 is composed entirely of elements essential for the human body, being intrinsically biosafe. ZX10's composition is distinguishable from other Mg alloys that contain rare-earth elements, such as yttrium (Y) [29] or gadolinium (Gd) [20], which may give rise to concerns, such as Y accumulation in bone tissue [30] or the possible generation of an adverse immunological response [31]. The wrought alloy ZX10 contains nanometer-sized intermetallic precipitates (IMPs), which govern its degradation behavior and are important in grain-growth restriction dur-

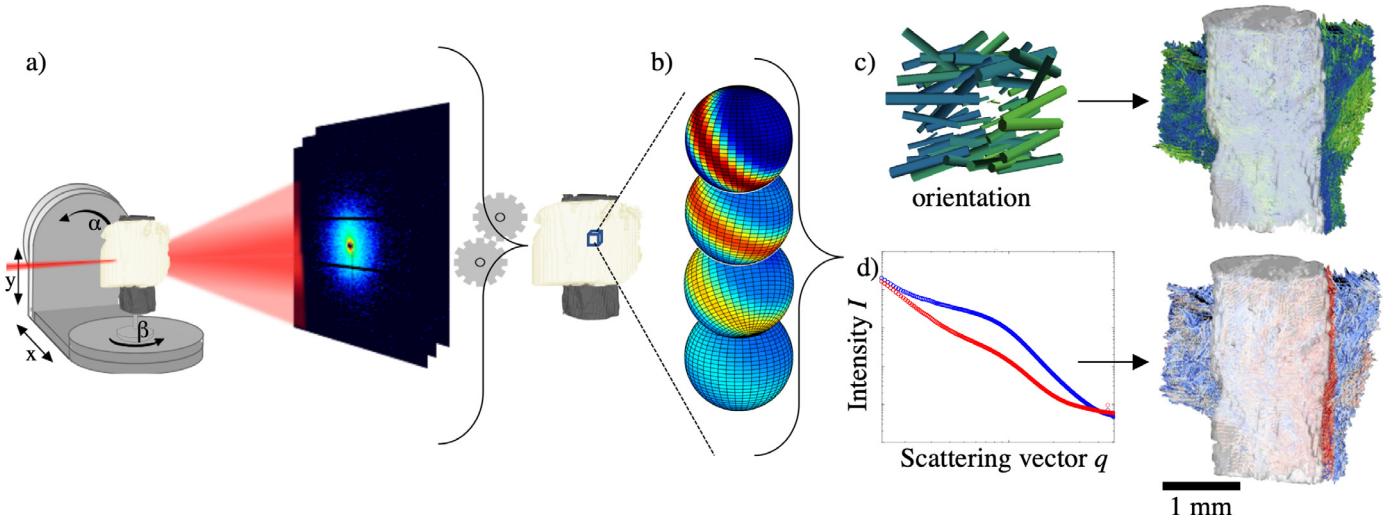

Fig. 1. Data acquisition, processing and visualization pipeline. (a) SASTT datasets require raster scanning of the sample in the x-y plane and the collection of subsequent projections at various rotation angles, β, and tilt angles, α. (b) After aligning the projections and reconstructing the tomogram, a 3D reciprocal space map is reconstructed for each voxel of the sample. (c) The reciprocal space map provides the vectors that indicate the orientation and degree of orientation (DOO) shown in a green-blue color code. (d) The reciprocal space map also provides the average scattering curve in that voxel and the low-q exponent, which is shown in a red-blue color code.

ing the production process and thus for its improved mechanical properties. Its detailed biodegradation behavior, the role of the intermetallic particles [32] and its susceptibility to stress-corrosion cracking and corrosion fatigue [33] have been studied *in vitro* in simulated physiological environment. Furthermore, its adaptation to bone has also been documented recently via a long-term *in vivo* study [32].

Here, we present new insights into the interactions between degrading Mg implants and bone nanostructure. We aim to address the following question: How does the implant degradation process affect the bone nanostructure in 3D at the bone-implant interface and its vicinity? We investigate the degradation process and the subsequent bone healing for a biomedically relevant ZX10 implant in a rat femoral bone using scanning electron microscopy, elemental analysis, and small-angle X-ray scattering tensor tomography (SASTT). SASTT yields the full scattering reciprocal space map for each voxel of a three-dimensional sample with high spatial resolution (Fig. 1). The localized nanostructural bone changes can be observed, quantified and put into their anatomical context. We also spatially resolve the bone-implant degradation layer, which is rich of degradation products as evaluated from the scattering patterns. By performing our investigations on bone samples at 3 different time points after implantation, we are able to follow the changes of the bone nanostructure as a function of time and observe distinct orientation patterns.

2. Materials and methods

2.1. Samples

In this study we used implants made from high-purity magnesium, alloyed with zinc and calcium to synthesize the alloy Mg-Zn1.0-Ca0.3 (in wt%). After solution and aging heat-treatments, indirect extrusion was performed at 325 °C to generate ZX10 rods of 3 mm diameter. Further details on materials synthesis and processing can be found in [32,34]. Pins of 1.6 mm diameter and 8 mm length were machined using polycrystalline diamond tools, taking special care to avoid any kind of surface contamination. The pins were cleaned using ultrasonic waves, air dried in clean-room atmosphere, and packaged airtight. Sterilization was performed by gamma irradiation at 51 kGray. The outer packaging prevented corrosion attack prior to implantation.

Femoral bones of 5-weeks old male Sprague-Dawley rats were investigated as model system. These young rats enabled the investigation of the whole implant degradation cycle of about 18 months within the same animal model. The cylindrical pins were inserted into a prepared transcortical implantation bed, drilled with ascending size up to the nominal diameter, with the rats under general anesthesia. The implants were inserted by gentle tapping to ensure a uniform press fit (Fig. 2). Postoperatively, the rats were allowed to move freely without external support and unrestricted weight bearing. After euthanization, the femurs were harvested and all adhering soft tissue was removed. The bone implant specimens were fixed in neutral-buffered 4% formalin solution. The entire surgical procedure, the post-operation treatment and the final euthanization step for explant analysis are described in [29]. The animal experiments were performed according to approved ethical standards and authorized by the Austrian Ministry of Science and Research (accreditation number BMWFW-66.010/0122-WF/V/3b/2014).

After explantation, the femoral bones with the overgrown implants were embedded in PMMA resin ('Technovit 7100', Heraeus Kulzer, Wehrheim, Germany) and the whole blocks were scanned via X-ray microtomography (µCT) to detect the degradation state and implant location. Representative samples were selected based on the µCT data and milled into cylinders of 3 mm diameter using a Struers Accutom 50 saw with a diamond polishing wheel. Figure S1, Supplementary Information, indicates the sampling sites. Bone samples containing a bioresorbable ZX10 Mg implant at progressing degradation stages (1 month, 6 months and 18 months after implant placement) and control samples, in which a hole was introduced in a similar position but without an implant (sampled 1 month and 6 months after surgery), were investigated. All samples originated from different animals. The implant samples stem from the right femurs of the animals while the sham samples originate from the left femurs.

2.2. X-ray microtomography data acquisition

µCT data were acquired using a Siemens Inveon Acquisition Workplace 1.2.2.2 in cone-beam geometry. Scans were carried out at 80 kV voltage, 500 µA current and 1050 ms exposure time per projection. A total of 180 projections over 210° were collected. The

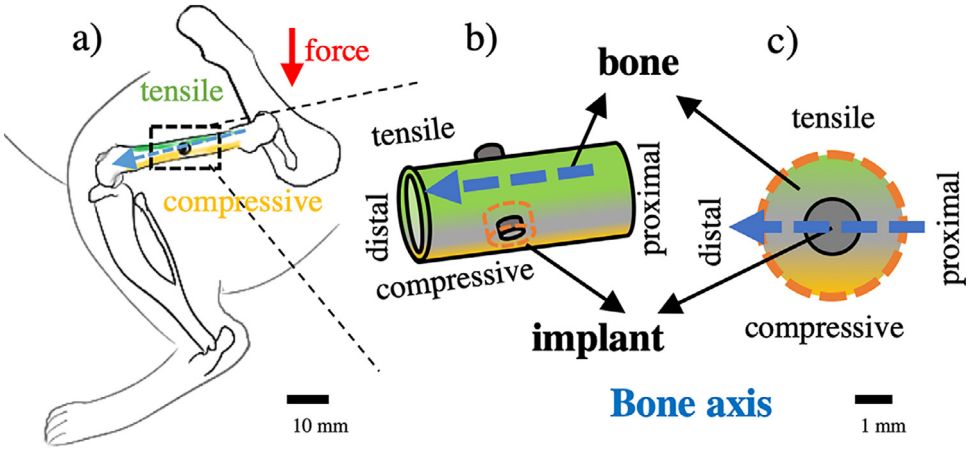

Fig. 2. (a) Sketch of implant position and load distribution in a rat bone with respect to the main bone axis (blue arrow from proximal side close to the hip to the distal side close to the knee). (b) Schematic sketch of the femural shaft with the implant pin being placed in penetrating fashion from one lateral side of the shaft to the other. The upper and lower part of the bone shaft are denoted tensile (green) and compressive (yellow) zones in bending. The SASTT sample is extracted from one lateral side as a cylinder containing the implant and surrounding bone tissue (orange dotted cylinder) (c) Face view of the SASTT sample with the implant pin in the center and the surrounding bone. The sample comprises mostly tissue from the lateral sides and some tissue from the tensile and compressive zones (upper and lower side, denoted as tensile and compressive, respectively). The blue arrows in (b) and (c) denote the bone axis in proximal to distal direction. The orientation in (c) corresponds to that of Fig. 3a-c and Fig. 4.

3D data were reconstructed using a filtered backprojection algorithm, resulting in a voxel size of 18.9 µm.

2.3. SASTT measurements

SASTT provides volumetric nanostructural information, such as the main scattering direction and degree of orientation (DOO) as well as the scattered intensity for each voxel of the tomogram. The SASTT experiments were carried out at the cSAXS beamline of the Swiss Light Source (SLS) at the Paul Scherrer Institut, Villigen, Switzerland. A schematic overview of the experiment and data processing pipeline is presented in Fig. 1. An X-ray energy of 18 keV was selected using a Si (111) double crystal monochromator and focused to a beam spot size of 50 µm by the combination of a horizontally focusing monochromator and a vertically focusing mirror. The bone samples were mounted on a steel needle and aligned to the center of rotation of a two-rotation-axis setup, which allows for tilt α, rotation β, and x-y translation scanning of the sample (Fig. 1a). The sample was mapped with a resolution of 50 µm. An exposure time of 0.03 s was used per scattering pattern, applying fly scans in the x-direction; x-y projections were taken for 10 different tilt angles α between 0 and 45°, and for rotation angles β between 0 and 180° for $\alpha = 0°$, and between 0 and 360° for $\alpha \neq 0$. The number of rotation steps per tilt angle was reduced by a factor of $\cos(\alpha)$ to provide equal angular sampling at different tilts [35]. The exact experimental parameters for each sample are listed in Table S1, Supplementary Information.

The SAXS patterns were measured using a Pilatus 2M detector [36] with a sample-detector distance of 2 m, which covers a scattering vector (q) range from 0.1 to 5 nm^{-1}, with $q = \frac{4\pi}{\lambda}\sin\theta$, where λ is the wavelength of the X-rays, and θ is half the scattering angle. A beamstop was used to block the directly transmitted X-ray beam. The sample transmission was measured using a diode mounted on the beamstop and the former was used to correct the scattering signal [37], as well as to reconstruct the absorption tomogram.

2.4. Reconstruction of SASTT data

The data were integrated by cSAXS Matlab routines into 980 radial and 16 azimuthal bins [38]. The alignment of the projections, based on a reference tomogram at $\alpha = 0°$, and the subsequent SASTT reconstruction were carried out within $q = 0.43$–0.72 nm^{-1}. Details of the SASTT reconstruction procedure can be found elsewhere [35]. Briefly, the reciprocal space map in each voxel is described by a series of spherical harmonics of orders $m = [0,0,0,0]$ and degrees $l = [0,2,4,6]$ and a zenith orientation parameterized with the spherical angles θ and ϕ.

The choice of even numbers for degrees l and zero-order m is based on the expected rotational symmetry of the collagen mineral composite around the collagen fibril axis, assuming that the mineral particles are all aligned with their long axis parallel to the collagen fibrils, but are randomly rotated around the fibril axis. This assumption is valid at the scale of the beam size (tens of micrometers), as we average over millions of mineralized collagen fibrils and about 10^9 mineral particles in each voxel of $50 \times 50 \times 50$µm^3 [6,24,26,35]. These l and m coefficients were optimized using a stepwise approach as further described in Ref. [35]. The error of the 3D reconstructions between the measurements and the projections is calculated from the reconstruction estimate, as given in Eq. (4) in Liebi et al. [35].

From the reconstructed reciprocal space map per voxel, the direction of the long axis of the collagen mineral composite and the DOO were extracted, as illustrated in Fig. 1c. The DOO is hereby defined as

$$\mathrm{DOO} = \frac{A}{A+B}, \tag{1}$$

where A is the anisotropic intensity in the spherical harmonics components and B is the isotropic scattering component of the spherical harmonics, in analogy to Pabisch et al.[39] for the case of 2D scattering. For the mathematical expression of the DOO in terms of spherical harmonic coefficients, we refer to Ref. [35]. To highlight the extracted quantities for every voxel, a small subvolume is shown in Fig. 1c, which reveals the orientation (via the orientation of the glyph) and the degree of orientation (in color code).

The absorption-based tomogram is reconstructed from the transmission signal, which was recorded by the diode mounted on the beamstop. For the q-resolved reconstruction, only the symmetric scattering intensity was considered in the SASTT code by optimizing the coefficients for $m = 0$, $l = 0$. This optimization was carried out for 200 log-spaced q-bins of the data, resulting in a one-dimensional scattering curve akin to conventional SAXS,

as illustrated in Fig. 1d. This approach was chosen for computational efficiency. We compared these simplified reconstructions to the full, higher-order orientation tensor, i.e. orders m = [0,0,0,0] and l = [0,2,4,6] and a zenith orientation parameterized with the spherical angles θ and ϕ. The obtained angularly averaged intensity was comparable for each q-bin and did not change the fitted values (see SI, Figure S2). This approach is comparable with conventional diffraction CT [23,40–42] or small-angle scattering CT [37], as it backprojects the intensity as a scalar quantity. All the projections recorded under tilt angles α were used to reconstruct the volume, leading to the average azimuthal scattering of the 3D reciprocal space map. In contrast to SASTT, this reconstruction aims to refine a single scalar quantity in the form of the scattered intensity as a function of the scattering vector q (Fig. 1d), in order to use established models [39,43] for fitting the scattering curves.

2.5. Fitting of scattering curves

The analysis of the reconstructed scattering curves allowed us to distinguish the scattering of the implant degradation layer from bone scattering with a power-law fit to the Guinier region [44]. Briefly, it allows to draw conclusions on the shape of large scattering structures in the system. The intensity decay takes the form

$$I(q) = aq^{-G}, \tag{2}$$

where $I(q)$ is the scattered intensity as a function of the scattering vector q, a is the scattering amplitude and G is the exponent. For the power-law decay fit, a q range between 0.3 and 0.7 nm^{-1} was used, as shown in the SI, Figure S3a. The fitting was implemented with the lmfit python package using a Levenberg-Marquard algorithm. With this fit and the different slopes, we were able to discriminate well mineralized bone from the degradation layer (Fig. 1d).

The particle size of the mineralized bone portion was calculated from the azimuthally averaged intensity $I(q)$. Assuming a two-phase system with a mineral fraction of 50% [45] and predominantly platelet-shaped particles, the parameter T was calculated as

$$T = \frac{4J}{\pi P} = \frac{4}{\pi P}\int_0^\infty q^2 I(q)dq \tag{3}$$

from the Porod constant P and the Invariant J. The Porod constant was determined from the region q = 0.9 to 2.3 nm^{-1}, extracted from the data presented in a Porod plot, Iq^4 vs. q^4 (see SI, Figure S3b). A linear fit was extrapolated to $q = 0$, which determines the Porod constant (red line in Figure S3b). The invariant J was determined from the Kratky plot, Iq^2 vs. q (see SI, Figure S3c), by integrating the scattering curve in the accessible q-range and by extrapolating it linearly to $q = 0$ and with q^{-4} to $q = \infty$. The determination of such parameters follows the approach by Pabisch et al. [39].

To calculate such parameters as a function of the distance to the implant surface, the absorption tomogram was segmented for air, bone, and implant. Hereby, the implant surface was selected as the outermost layer of the reconstructed implant volume at this degradation state. As the implant surface location changes due to the ongoing degradation process it renders comparison of different degradation states difficult. We thus decided to estimate the implant center location from the remainder of the implant by first determining the implant's center of mass in each tomographic x-y slice along the implant direction. Then the center x-y coordinates were fitted using a linear regression to determine the implant center in 3D. We found this estimate to be robust against uneven implant degradation. The Euclidian distance was then used to calculate the closest distance to the implant center for each voxel.

2.6. SEM/EDX data acquisition

The scanning electron microscopy (SEM) and electron dispersive X-ray spectroscopy (EDX) data were acquired with a FEI Quanta 250 FEG. The samples were investigated after the SASTT experiments and re-embedded with an epoxy resin (Agar LV resin) to facilitate handling and cutting with a diamond wheel using a Struers Accutom 50. The sample surface was subsequently polished with 0.1 µm alumina suspension. The samples were at first left unsputtered for backscattered electron imaging (BSE) and EDX analysis, and the SEM was operated in low-vacuum mode at 130 Pa. The acceleration voltage was 20 kV. The EDX data was acquired with an EDAX Octan SDD detector at an exposure time of 1000 µs and 100 repetitions. Subsequently, the samples were sputter-coated with carbon and reinvestigated via secondary electron (SE) imaging in high vacuum at an acceleration voltage of 5 kV. The EDX data is presented in a qualitative fashion by showing the peak intensities rather than the concentrations, as the unknown and varying sample compositions result in strong energy-dependent absorption of the emitted X-rays. The latter produces large uncertainties in these absorption effects and thus does not allow for a proper elemental quantification.

2.7. SEM data treatment

The BSE data were segmented using a trainable machine-learning algorithm (Trainable Weka Segmentation) [46], implemented in the Fiji image processing package. A training dataset was built by a manual selection of the relevant structures (bone, implant, lacunae and background), and the whole image containing the full sample cross-section was segmented by this approach. This segmentation was further used to calculate the lacunar density in Matlab.

2.8. Statistical analysis

The box-plot representation in Fig. 5 was chosen to reveal the obtained parameters as a function of distance from the implant. It shows statistical parameters such as the median (red line in the center of the box), interquartile range (size of the blue box), and the range of 1.5 times the interquartile range (dashed lines).

A one-way analysis of variance (ANOVA) with a Bonferroni test was used to determine statistically significant (significance level = 0.05) differences between successive box plots. For this, the box plots were compared to the respective neighbors. Significantly different neighbors are marked with stars in Fig. 5 and the significance between the different time points is presented in the SI, Figure 9. This procedure was implemented in Matlab.

3. Results

Fig. 2 sketches a rat femur with an implant (Fig. 2a). The blue arrow points from the proximal to the distal side of the bone shaft and denotes the main (longitudinal) bone axis (Fig. 2b). Fig. 2c represents the extracted sample and indicates the presumed zones of different mechanical stress, as zones of tensile (top) and compressive (bottom) stresses. We describe the reaction by four different quadrants: distal, proximal, tensile and compressive sides (Fig. 2c). We introduce a reference vector along the proximal-distal direction, which corresponds to the long axis of the femur (blue arrow in Fig. 2c). The implant/hole placements and the regions from where the SASTT samples have been extracted are shown in *ex vivo* μCT scans in the SI, Figure S1.

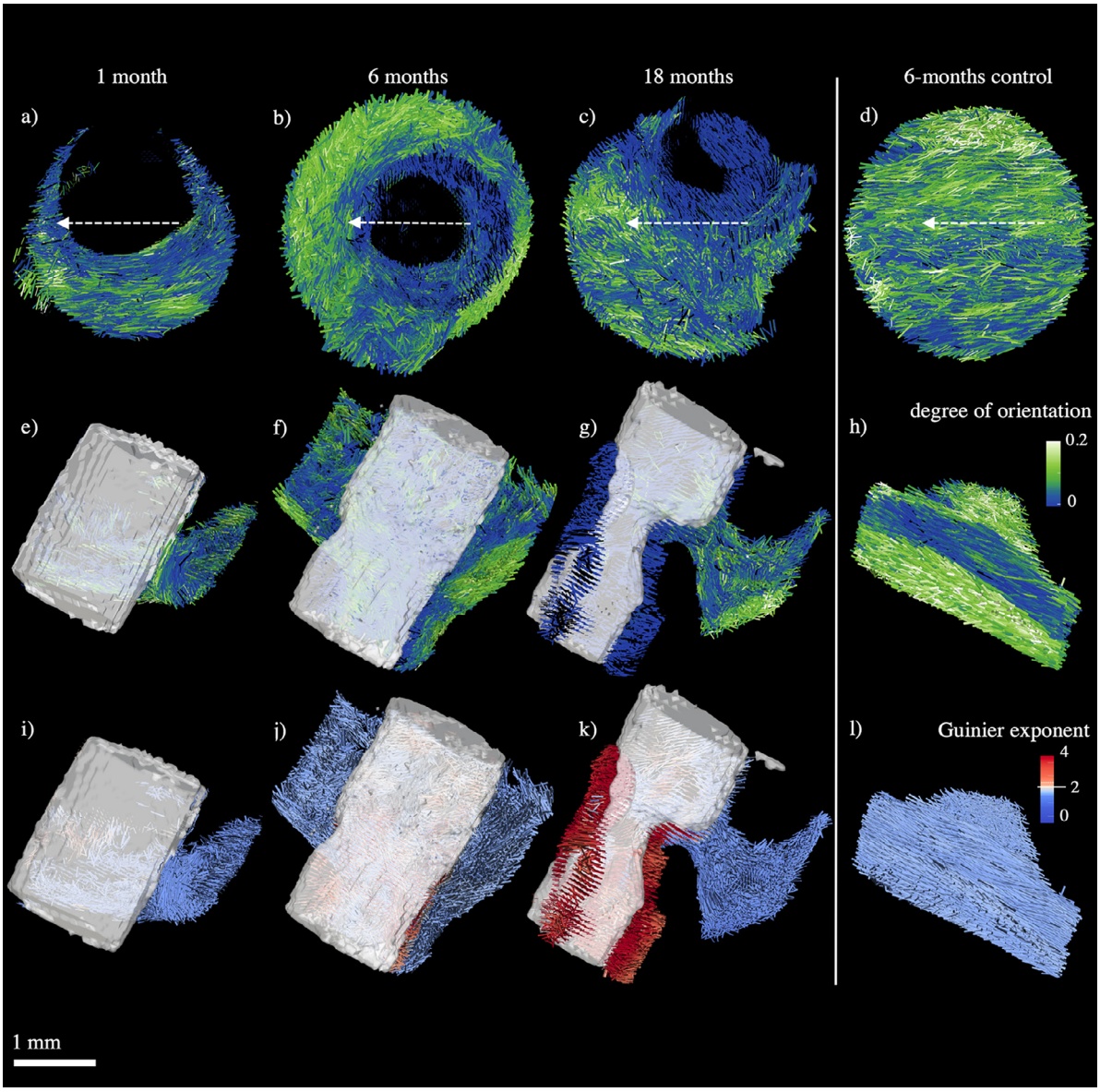

Fig. 3. SASTT reconstructions represented by glyphs. Reorientation of bone nanostructure around a slowly degrading Mg implant (shown in white), from left to right columns: 1 month, 6 months, and 18 months after implantation, plus a control sample 6 months after receiving sham treatment. The control sample after 1 month is presented in the SI, Fig. S4. The arrows in (a-d) depict the long-bone orientation along the proximal-distal direction. The colors of the glyphs represent the degree of orientation (a-h) and the low-q Guinier exponent (i-l), respectively. The Guinier exponent shows higher values at the degradation layer of the bone-implant interface. The glyph length correlates to the symmetric scattering intensity in all cases.

3.1. Orientation information from SASTT

From the SASTT reconstructions of the 3D reciprocal space map we obtain the preferred orientation of the collagen-mineral composite in bone in every voxel. Fig. 3 shows simultaneously the orientation per voxel along the direction of the glyph, the scattered intensity via the length of the glyph, and the degree of orientation (Fig. 3a-h), or the low-q Guinier, G, exponent (Fig. 3i-l), via the green-blue or red-blue color coding of the glyph. The exponent G allows to distinguish fully mineralized bone tissues with $G \leq 2$ and more compact structures, such as the degradation layer and non-mineralized tissue, with $G > 2$.

Viewing the sample along the axis of the cylindrically shaped implant in Fig. 3 a-d enables to see the structural changes along the implant direction. The blank space in the center corresponds to the implant locus, which was removed for ease of viewing the portion of forming bone inside the original implant diameter, and the white arrows indicate the longitudinal bone axis, pointing in proximal-distal direction (corresponding to the blue arrow in Fig. 2). In contrast, Fig. 3 e-h shows the tomogram viewed perpendicular to the implant axis, which enables to see changes at the bone-implant interface. Here, the remaining implant is displayed in white, and its shape is obtained from the absorption tomogram. The respective graphs of the control sample after 1 month are presented in the SI, Figure S4. The collagen-mineral composite in the rat femur shaft is generally co-oriented along the main load direction, i.e. in the longitudinal axis of the bone shaft. The orientation gets perturbed by the insertion of the Mg implant, which could be visualized here for the first time in 3D. As the Mg implant shrinks due to bioresorption, the alignment of the collagen-mineral composite in the long-bone direction, as determined from the nanostructural parameters obtained by SASTT, is slowly regained.

The local deviation of the mineral particle orientation from the regular direction along the bone axis can be quantified by relat-

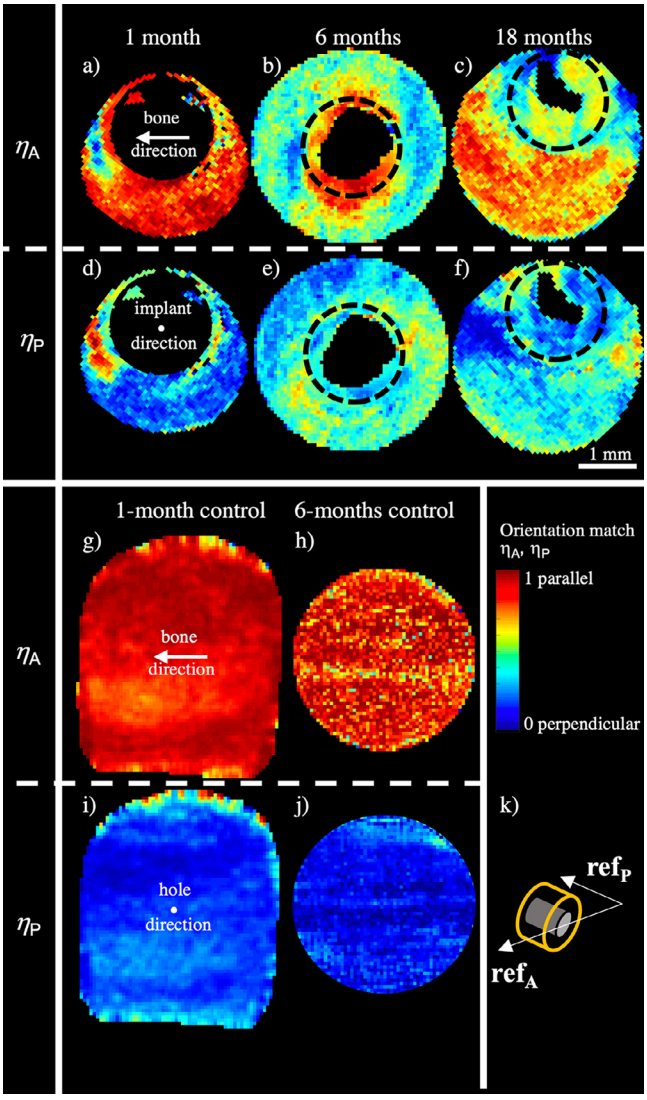

Fig. 4. 2D maps showing the orientation match parameters η_A and η_P as a function of position in the plane perpendicular to the implant direction (sample cross-section). Upper panel: samples with implant; (a-c): η_A, (d-f) η_P. Lower panel: control samples (sham); (g-h) η_A, (i-j) η_P. The initial implant diameter is indicated by black circles. The η_A and η_P values are displayed in color code and the reference system with the bone axis (ref_A) and the implant pin axis (ref_P) is schematically sketched in (k).

ing the mineral particle orientation to a reference vector. In this work we used the normalized dot product between the nanostructure orientation and a reference vector to yield a local orientation match parameter η with values between 0 (bone nanostructure orientation perpendicular to the reference vector) and 1 (bone nanostructure parallel to reference vector). The analysis was carried out including $G > 2$ voxels because the degradation layer does not exhibit a preferred orientation. This does not alter the analysis where partial volume voxels are presented. The analysis was performed for the longitudinal bone axis (arrows in Figs. 2 and 3) as reference, yielding a map of local orientation match parameters, η_A, with respect to the bone axis. The analysis was also performed for the implant pin axis as reference, yielding a map of orientation match parameters, η_P, with respect to the implant direction (Fig. 4k). In order to obtain meaningful trends, the η_A and η_P values were averaged along the implant pin axis and displayed as 2D maps, with the hole in the middle representing the implant location (Fig. 4a-f). Furthermore, orientation match parameters were calculated for the sham samples (control group, Fig. 4g-j). In this case the direction of the hole was taken as implant direction for reference. Since the hole in the sham samples had healed very quickly, its direction is not visible any more but had to be extracted from *in vivo* CT data taken after implantation.

In the control group (sham), the alignment of the mineral particles is parallel to the long-bone direction throughout the whole sample volume (Fig. 4g-h, high η_A values). No re-orientation towards the drilling direction is observed (Fig. 4i-j, low η_P values).

For the 1-month sample with implant (Fig. 4a), η_A is mostly close to 1, similar to the control, indicating little deviation from the regular nanostructure orientation along the bone axis. Notable deviations are visible only in narrow zones at the proximal side and, even more pronounced, at the distal side (left-hand side of the sample), where η_A approaches 0 in a zone at about 400 µm distance from the implant. This means that in this zone the nanostructure orientation is almost perpendicular to the regular direction along the bone axis. This is further confirmed by observing the orientation match parameter η_p with respect to the implant direction (Fig. 4d). Areas of high η_P coincide with areas of low η_A, showing that in these areas the bone nanostructure has re-oriented in the direction of the implant rather than in that of the bone axis.

After 6 months, the η_A values are dramatically reduced throughout the sample, indicating a general loss of the regular orientation along the bone axis. Interestingly, this orientation change does not lead to high η_P values, which would indicate a preferred orientation along the implant pin. The η_P values are also low throughout the sample, which is consistent with a wrapping orientation of the collagen-mineral composite around the implant. Especially in the distal and proximal zones, large areas of realignment can be found. By contrast, some newly formed bone in this sample, which replaces the already partially degraded implant (tissue within the circular outline denoting the original implant in Fig. 4b,e), shows high η_A values, in particular on the top and bottom sides (compressive and tensile zones). In this narrow zone, the bone nanostructure appears to be strongly aligned along the main bone axis, much stronger than in the surrounding bulk.

After 18 months, the η_A values have increased again, indicating that the bulk of the sample regained a preferred orientation in the regular direction. Only the distal and proximal zones still show somewhat lower η_A values (Fig. 4c). Also, in the zones where the implant was replaced by bone the nanostructure shows some preferred orientation along the main bone axis. The η_P values remain low in the bulk of the sample, indicating no orientation along the implant axis, similar to the 6-months sample.

3.2. Nanostructural parameters from q-resolved reconstruction

In addition to the orientation information obtained via SASTT reconstruction at a fixed q value, we also applied reconstruction of the full scattering curves per voxel. Although the spatial resolution of the tomogram is still given by the voxel size, we were able to extract quantitative structural information at the nanometer scale (between 1 and 100 nm) in each voxel. For this purpose, we averaged the 3D directional scattering in each q-bin to obtain a 1D scattering curve of intensity vs. scattering vector q (Fig. 5a), akin to standard SAXS experiments. This allows to identify nanostructural parameters, such as the thickness of the mineral particle via calculating the so-called T-parameter [16] in each voxel.

Fig. 5a shows reconstructed scattering curves per voxel averaged within subvolumes of similar structure. It was found that the scattering curves from the control sample (grey) were very similar to those of bulk bone (blue), while the scattering curves in the implant degradation layer (red) at the implant-bone interface differed markedly from the rest. The shoulder at around 1 nm^{-1}, formed by the scattered intensity plotted as a function of q, is associated

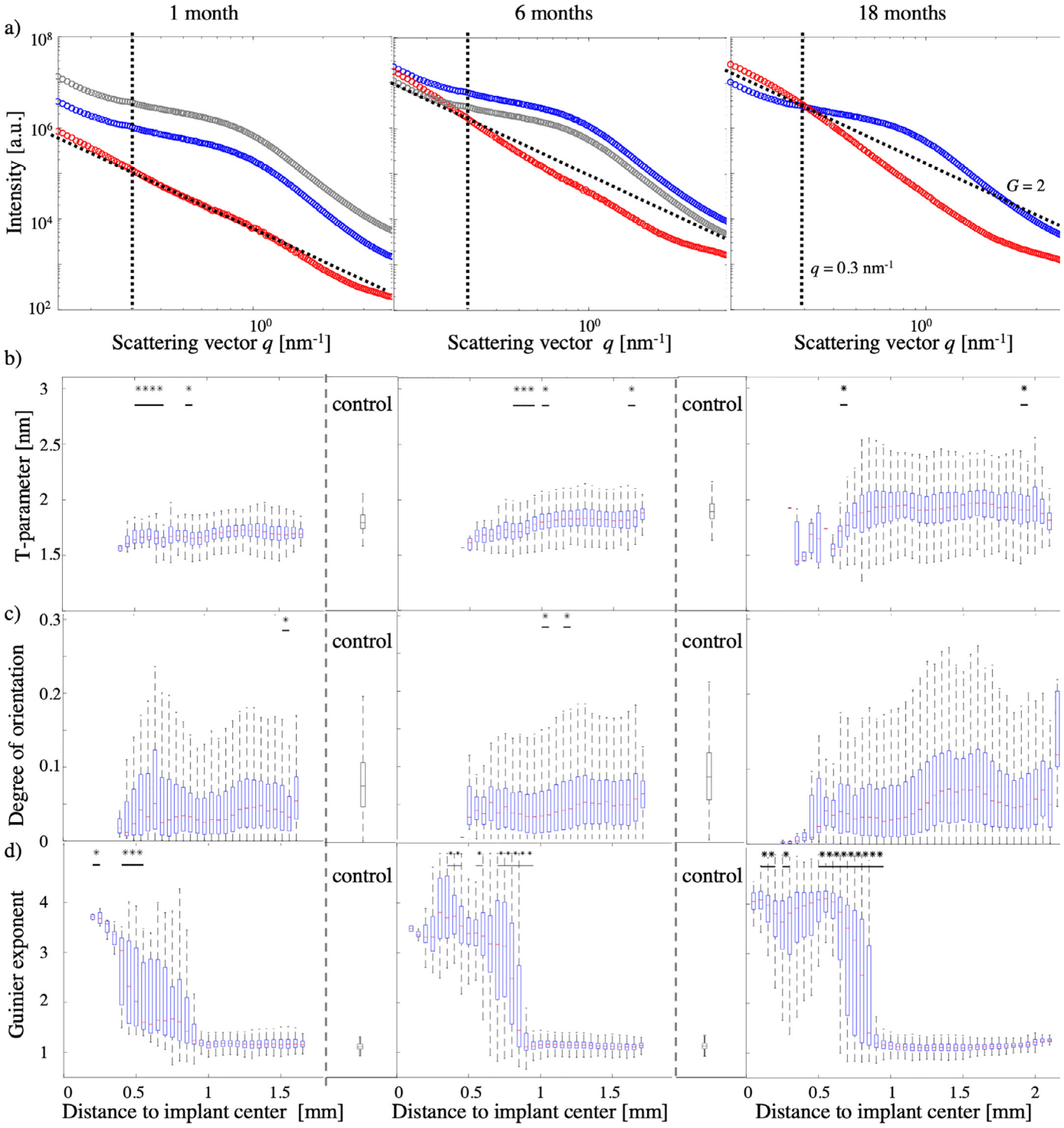

Fig. 5. (a) Reconstructed scattering curves per voxel close to the bone-implant interface (red) and into the bulk of the bone (blue) at three different time points (1, 6 and 18 months), and for the control (grey) at 1 and 6 months. (b,c) Boxplots of the T-parameter (b), the DOO (c) and the Guinier exponent (d) presented as a function of distance from the implant center. For 1 and 6 months, boxplots of the average T-parameter (b), DOO (c) and Guinier exponent (d) are also shown for the control samples. Stars above the boxplots mark significant differences between two neighboring groups. The original (undegraded) implant extended to an implant-center distance of 0.8 mm. The slope at $q = 0.3$ nm^{-1} (dotted vertical lines) was used to obtain the Guinier exponent G; for comparison, dotted lines with $G = 2$ are indicated in (a).

with the bone mineral particles. This shoulder is mostly absent in the interfacial bone-implant region. For all samples, the slope in the log-log plot at low q ($q < 0.3$ nm^{-1}) is referred to as G. The value of G in the degradation layer differs from that typically seen in bulk mineralized bone. While in bulk bone the exponent G usually takes values between 1 and 2 [17], G values above 2, represented by a red color in Fig. 3i-l, are found at the interface. This is clearly visible when plotting the G value as a function of distance from the implant center for all samples with an implant (Fig. 5d). By contrast, the control sample (Fig. 3l and SI, Figure S4) shows exponents $G < 2$. Since the T-parameter evaluation of mineral particle thickness is only valid for $G \leq 2$, voxels with $G > 2$ (indicated in Fig. 3 and Fig. 5a) had to be excluded from the T-parameter and DOO analysis in Fig. 5. Nevertheless, we presented the full range of

G values in Fig. 5d to reveal information on the degradation layer and newly formed bone. A statistically significant increase in the T-parameter can be observed over the three time points (see SI, Figure S9), which can be attributed to the growth of the animals and is also observed in the control samples (Fig. 5b, Fig. S9). This increase, however, goes together with a statistically significant local decrease of the T-parameter at the interface for all time points and a spread of the interquartile range about 1 mm away from the implant center after 18 months.

The DOO of bone increases gradually with the distances from the bone-implant interface. This gradient is more pronounced over time and goes also along with a spread in the interquartile range over time, but is only statistically significant in very few places. We observe that after 1 month, a very thin interfacial bone layer is formed around the implant (Fig. 3a). Within this layer, the mineral particle orientation deviates from the expected global orientation along the bone axis and has a lower DOO. The generally low DOO of this sample is in part also due to the young age of the rat, and consequently ongoing bone growth, and compares well with the DOO found in the 1-month sham sample (Fig. 5c, grey boxplot). The interfacial bone layer grows to about 0.5 mm with similar DOO after 6 months (see Fig. 3b,f and Fig. 5c). In fact, the 6-months sample shows a bulk altered orientation, while the strongest effect is visible at the bone-implant interface. In contrast to this altered orientation, the 6-months sham sample exhibits a rather strong orientation along the long-bone direction. The DOO after 18 months is generally higher compared to that of the 6-month implant sample, and only shows some reduction towards the medullary cavity. After 18 months (Fig. 3c,g), a distinct preferred orientation is regained, and disordered zones are mostly found in areas where the implant is replaced by new bone.

3.3. The interface layer

Using the information from the *q*-resolved reconstruction, one can combine it with the SASTT orientation information. In this way it is possible to visualize the interface layer characterized by a Guinier exponent of $G > 2$, as opposed to bone with $G \leq 2$. In Fig. 3i, it is clearly visible that in the 1-month sample the interface layer is mostly absent. It starts to appear in the 6-months sample (Fig. 3j) and is very pronounced in the 18-months sample (Fig. 3k). While the distinct difference shows that this layer is not bone, it does not unambiguously reveal its nature, whether it consists of implant degradation products or non-mineralized tissue. In order to characterize the interface layer further, we performed SEM/EDX measurements on the samples after the SASTT measurements.

Fig. 6 depicts the SEM analysis on longitudinal sections of the samples with a combination of back scatter electron (BSE) imaging (a) and energy dispersive X-ray analysis (EDX) (b-c). The BSE signal (Fig. 6a) allows us to visualize the bone morphology and mineralization process by showing the lacunae (white arrows) and observing zones of varying mineral density (SI, Figure S5, where prominent zones are marked with blue arrows). It is noteworthy that these zones are more prominent in the 1- and 6-months samples than in the 18-months sample. The overall lacunar density in the samples shows a slight decrease from 490 lacunae/mm^2 one month after surgery to 420 and 400 lacunae/mm^2 after 6 months and 18 months, respectively. Focusing on the implant-bone interface, a degradation layer is visible that is co-localized with areas of increased low-*q* exponent *G* (Fig. 3i-k). The BSE signal indicates a lower Z composition than in the bone matrix, but still significantly higher than in the surrounding embedding medium.

EDX was used in order to investigate the elemental composition of the bone-implant interface layer. The regions investigated by EDX are highlighted in the overview Fig. 6a with red rectangles. The rationale for the selection of the various zones was to have implant-bone interface and embedding resin in the field of view. The slicing plane was chosen to align roughly with the virtual cut presented in Fig. 3e-g. In Fig. 6b, Mg is shown in red, O in blue, Ca in dark green, C in purple and P in light green. These colors are overlaid to present their spatial distribution in the sample. In the first step, the composition of the resin matrix and unaffected bone (as far from the implant as possible) was analyzed to generate a baseline for the identification of the elemental composition. The resin contains mostly C and O, whereas bone is characterized by the presence of Ca and P. The EDX analysis of the degradation layer clearly allows to identify the Mg implant and the bone matrix from the strong signature of Mg and Ca, respectively (Fig. 6b). The degradation layer in direct contact with the implant (~20 µm thick) is characterized by a strong signature of O, very little Ca and P as well as a moderate amount of Mg. We thus conclude that this layer is composed mostly of $Mg(OH)_2$, a commonly found degradation product of Mg implant degradation [47,48]. Further away from the implant surface, we find a gradual increase in the Ca and P content over a thickness between 50 and 200 µm before their content reaches a plateau. This second layer seems to be composed mostly of Ca-phosphates and compares well with the literature reports of the degradation layer and the adjoining new-forming bone [10,13,14]. Ca- or Mg-phosphates at the interface have been characterized as apatite mineral by scanning WAXS [20], albeit that study could not find $Mg(OH)_2$. We suppose that this is caused by WAXS being rather insensitive to poorly crystalline or amorphous compounds and the fact that the lower electron density of Mg-hydroxides compared to Ca-phosphates, causes weaker scattering.

4. Discussion

4.1. Mineralization and growth

One parameter that is related to the maturation stage of bone is the thickness of the mineral particles, which is directly related to the T-parameter. The T-parameter extracted from the scattering curves is in the range of 1.5 to 2.5 nm, which is in good agreement with literature reports on healing bone [49], our own reports on Mg implants [21,50], and the control samples that were investigated in this study. In agreement with our previous studies, the T-parameter showed only mild changes, while other literature reported larger deviations during healing [51]. In this context, the deviations within individual samples, and the fact that the animals were still growing during the first six months of the study, also led to an increase in the T-parameter with time as visible in the control samples (Fig. 5b). As the classical calculation of the T-parameter is based on a mineralization degree of 50% and the developing bone might deviate from this, corrections were employed in several previous 2D studies. These rely on correlating the electron density derived from BSE imaging with the T-parameter and calculating a corrected parameter, usually denoted as W-parameter [45] and defined as $W = \frac{T}{2(1-\phi)}$, with ϕ the mineral fraction. As it is very difficult to obtain accurate mineralization densities for our 3D volumes, this correction could not be carried out in our case. However, as we are mostly concerned with lower mineralization levels in the early time points of this study, this lower mineralization will just lead to a slight overestimation of the mineral particle size.

Other factors to consider are the remodeling properties of rat bones, where the most notable difference between human and rat bone is the absence of osteonal remodeling in rats and the associated usually low intracortical remodeling activity [52–56]. Despite these shortcomings, reports on the suitability of rats as an *in vivo* model conclude that the animals' reactions towards the implant and the related morphological response give valuable insights into

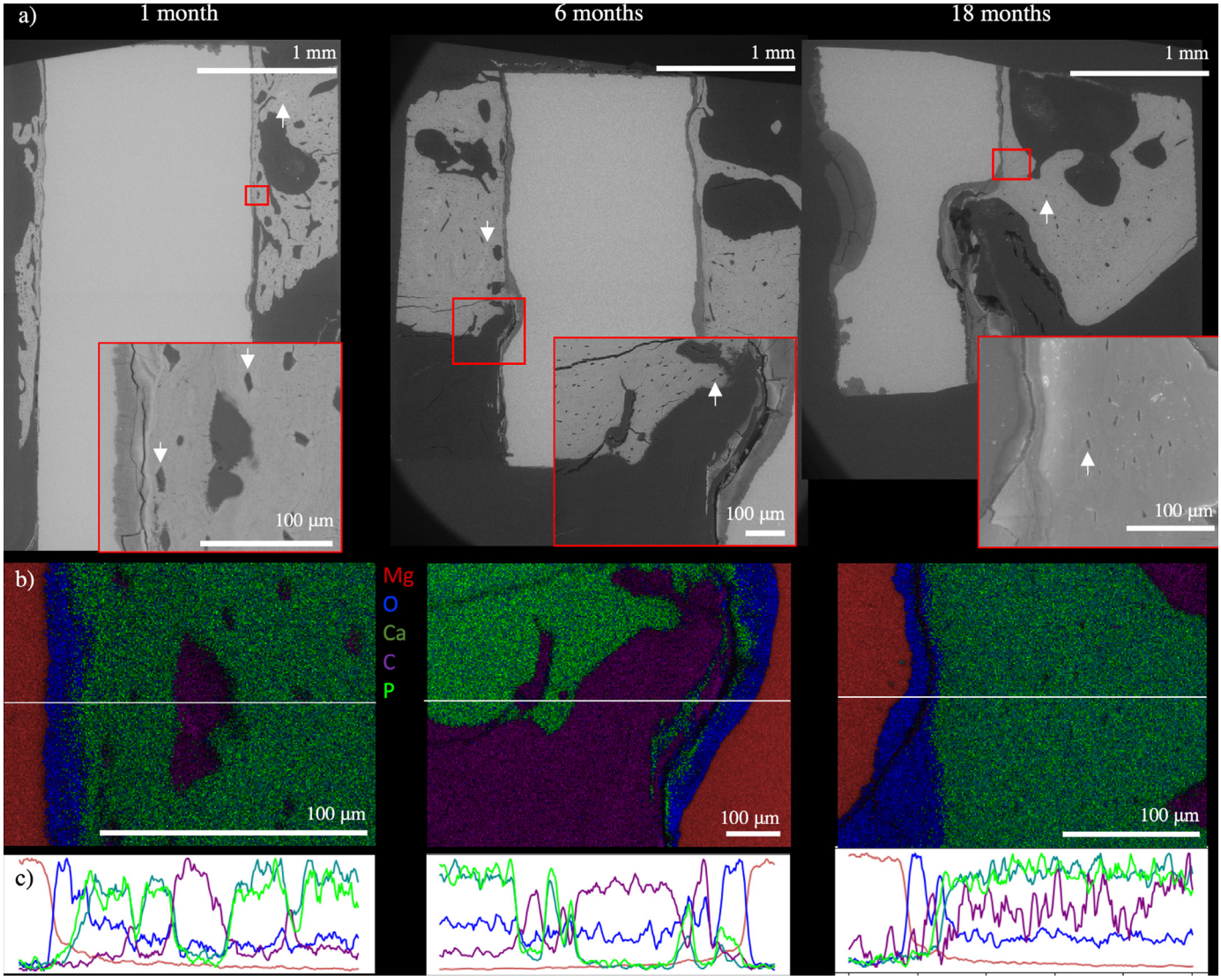

Fig. 6. Scanning electron microscopy of sample cross-sections. (a) BSE overview images showing the morphology of the bone around the central implant. Lacunae are highlighted by arrows. Red squares mark the area of the magnified interfacial region of implant and bone. (b) Corresponding EDX maps of magnified regions in (a), showing the elemental distribution at the bone-implant interface: Mg in red, O in blue, Ca in dark green, C in purple and P in light green. (c) Line profiles extracted along the white lines in (b), showing the degradation layer as Mg/O-rich and revealing a gradual increase in Ca/P content towards the bone.

the *in vivo* implant performance and the surrounding bone, respectively [57].

Through BSE imaging (Fig. 6 and SI, Figure S5), we can detect mineralization differences and thus follow the general bone development over time, displaying a gradual process from a woven-bone structure (1 month) to a more mature, lamellar bone structure (18 months). Furthermore, areas of active bone formation, indicated by localized mineral density differences in BSE imaging, are still visible close to the implant after 18 months (blue arrows in Figure S5). Globally, the lacunar density decreases with animal age, very similar to the process in human bone [58]. While lacunae are usually associated with osteocytic activity, SEM imaging cannot answer the question of whether they hosted viable osteocytes or not. The decreased lacunar density together with a more elongated shape and co-alignment of neighboring lacunae (Fig. 6) with progressing implantation time indicates a transition to a more mature bone [59]. This is in line with the generally lower DOO of the young rat (1 month after surgery) compared to later time points (6 and 18 months after surgery) found with SASTT (Figs. 3 and 5).

An interesting observation of this study is the visualization of the degradation layer, which is formed in place of the degrading implant and does not exhibit the typical scattering of the bone mineral. This layer grows over time to a thickness of 50–200 µm. The scattering from this layer was found to exhibit a higher exponent in the small-q region, namely $G > 2$, which points towards a rather irregular structure. The degradation layer is characterized by high levels of O and Mg, hence most probably a $Mg(OH)_2$ layer, which has been reported previously as the common degradation product [47,48] in the degradation layer around Mg implants. Notably, P is mostly absent in the degradation layer, which is consistent with the absence of phosphates. Further SEM investigations of the interface show a fibrous structure with granular patches (see orange arrows in panels (c) and (d) of Figures S6-S8 in the SI). These zones, which exhibit a typical feature size of about 300 nm, are particularly prominent in the 1- and 6-months samples. We hypothesize that these are $Mg(OH)_2$ particles formed by implant corrosion and are not biogenically formed apatite particles due to the absence of a bone-like mineral particle shape in the SAXS region. Nevertheless, further WAXS investigations would be needed

to gain more detailed information on this issue. It is important to exclude these zones from the further analysis of the DOO and T-parameter.

The degradation layer is well-known to occur around degrading Mg implants and has been characterized by tomography methods [60–62], 2D X-ray scanning diffraction [20], and electron microscopy approaches [10,63]. SASTT is able to give new insights into the degradation layer's 3D structure and scattering behavior together with observing bone growth around the irregularly shaped implant remainders. By contrast, such an interface is difficult to detect via 2D scanning SAXS, because it is rather thin and not continuously present around the implant. Therefore, it has not been detected in the slice geometry of earlier studies [50], although other work [10] identified a chemically different, amorphous calcium phosphate interface and ascribed its formation to the osteoinductive properties of Mg. It is in fact a strength of SASTT to give insights into complex arrangements, such as pockets formation inside pits of degraded implant material, which can subsequently mineralize.

4.2. Orientation

Orientation analysis allows to track the changes of the nanostructural orientation over time. Here, it is important to consider the mechanical load situation of bone and how this influences the stress distribution around the implant. The mechanical optimization of bone is a research topic of significant interest and there is general consensus that bone adapts to the current load situation and that abrupt alterations in the load pattern (such as fractures) change the stress distribution and provoke a change in the nanostructure [49]. Re-orientation effects around implants have also been observed with SAXS [18]. In fact, it is well known that prolonged alterations in the stress distribution can lead to problems such as stress-shielding phenomena caused by a mechanical mismatch of the implant and bone moduli [64]. This may be less of a problem in the case of Mg, since the moduli of Mg and bone are quite well matched [48]. Nevertheless, the implant pin placement can be assumed to considerably change the loading pattern. While it is difficult to control the loading patterns, duration, or exact implant location in *in vivo* studies, it is reasonable to assume a compressive/tensile zone from the animal anatomy, the walking activity of the animals, and the force due to gravity. Fig. 2 illustrates this assumption for the predominant load situation in intact bone, whereas the presence of the implant or associated hole might change this loading pattern.

In this study, we observe orientational differences between the mineral particles in the proximal/distal zones in the samples with implants, but not in the sham samples. We therefore interpret these findings as a distinct reaction of the bone to the presence of the implant, rather than a generic healing response to the insertion of a hole. An initial reaction is observed after 1 month, likely triggered by the modified loading situation and bone healing since the implant degradation is still minimal. Narrow areas at the proximal and distal sides exhibit a nanostructure that is not aligned with the bone axis (Fig. 4a) but aligned along the implant direction (Fig. 4d). Previous observations made by 2D SAXS [50] revealed a bony bridge that formed between the two cortical sides. The here observed zone with an orientation along the implant direction is interpreted as the same feature on one cortical side. As the implant degradation sets in and the animals grow, at 6 months after implantation a wrapping of the mineral-collagen composite around the implant can be observed in a zone of up to 1 mm away from the implant (Fig. 4b). This is accompanied by an overall reduction of preferred orientation (Fig. 4e) along the implant direction, and might be interpreted as a mechanical adaptation that reduces the anisotropy in this direction. After 18 months, we see a return to the preferred orientation along the bone main axis, i.e. the regular direction in intact bone (Fig. 4c).

With the limited number of samples, we can only speculate on possible mechanisms that drive the nanoscale adaptation. Two major stimuli are identified, which are on the one hand the surface chemistry of the implant and on the other hand the load conditions that are modified due to the implant placement and its subsequent degradation. While the surface's chemical composition can have a large impact on the growth properties, this effect is expected to be most pronounced for the case of calcium phosphate surfaces [65]. In fact, a recent study using scanning SAXS/WAXS did not show significant differences in the DOO or mineral particle thickness between different implant materials such as Ti, PEEK, or Mg–Gd alloys [20].

The second important factor to consider is the mechanical regime. It has been demonstrated by *in vitro* experiments that osteoblast cells can align parallel to a surface or the direction of an applied mechanical stimulus, e.g. in response to cyclic stretching or fluid flow [66]. Aligned osteoblasts were shown to produce a highly orientated extracellular matrix (ECM) with collagen fibers aligned in the same direction as the osteoblasts [67]. In bone, the situation is more complex, with osteocytes playing an important role as mechanoreceptors and likely also as mediators for the 3D organization of the ECM [68,69]. Mineralization of collagen fibers is known to be highly controlled by collagen fibrils as a molecular template [70], resulting in elongated HAP particles aligned parallel to the collagen fiber axis, with the crystallographic *c* axis also pointing in longitudinal direction.

We assume that the guidance by the implant surface and mechanical stimuli is a major trigger for the collagen/mineral reorientation observed in this study. The importance of mechanical triggers in bone around implants was also illustrated in a study investigating, among other parameters, the collagen/mineral orientation around implants in rabbit tibia by polarized microscopy [71]. The authors found that the orientation of collagen fibrils in the vicinity of the implant was altered when the implant was loaded cyclically. It should be noted, however, that a purely mechanical view might be too limited, since also wound healing processes take place. In healing bone, disordered collagen fibers are typically deposited first (woven bone), which are later replaced by orientated collagen fibers in a remodeling process. Due to the continuously changing healing front adjacent to a degrading implant and remodeling further away from it, these two processes are expected to happen in parallel. One may speculate that the initial response, i.e. the orientation of collagen fibers along the implant axis and the formation of a bony bridge, is mainly governed by surface stresses induced by the implant. In the second stage the void created by the degrading implant has to be filled with bone tissue. To our knowledge, the "wrapping pattern" in this stage has not been observed before and may have several reasons, such as a characteristic corrosion surface triggering the alignment of fibers in a circumferential way or local mechanical stresses that may be created by the corrosion process (gas formation) and potential inflammation. One can further speculate that re-orientation in the direction of the main loading axis (longitudinal bone axis) starts only after these additional effects have subsided, therefore an intermediate stage may be considered that also influences the mechanical stability during this time.

4.3. 2D scanning SAXS and SASTT

As we have shown, there are clear advantages in the nondestructive 3D characterization of the sample over the analysis of thin 2D slices with scanning SAXS. [68,71–73]. This is specifically the case for an implant in an advanced degradation state as SASTT provides more significant information on the sample volume, its

spatial variation, and the 3D nanostructure anisotropy. For more complete studies with 2D scanning SAXS at least three orthogonal 2D slices (sagittal, coronal and transverse) through the implant would be needed to allow judging the mineral orientations around the implant and their spatial variation. This would necessitate three individual samples and increase considerably the study's biological variability. An additional complication when using slices is to preserve thin and fragile interfaces while producing sufficiently thin sections with thicknesses comparable to the beam size over the whole sample area. Non-destructive tomographic methods have a distinct advantage, especially when irregular and strongly degraded implants are to be investigated and a high spatial resolution is needed.

While many studies are carried out via 2D scanning [20,21,50], it should be noted that the obtained information retrieved from the 3D nanostructure anisotropy is incomplete. Since only a 2D cut of the 3D reciprocal-space map is probed, analysis of this data should be done under careful *a priori* assumptions on the orientation of the 3D nanostructure because the out-of-plane orientation cannot be probed. In order to recover the 3D nanostructure anisotropy and avoid these assumptions, a thin sample may be scanned at several incidence angles in order to reconstruct the local 3D reciprocal-space map [72].

Another important point of comparison is the possibility of induced mechanical damage, which does not occur in SASTT due to its non-destructive nature. We have experimentally observed that the scattering signal in the low-q region can be affected by cutting artefacts [73]. These problems are to some degree expected for any mechanically invasive method, since cutting or polishing may alter the related structure, in particular when the slices become very thin, which is needed for high resolution, and if there are strong material heterogeneities at play, which is the case for an implant-bone system.

One notable disadvantage of SASTT is the prolonged measurement time. In 2D scanning SAXS, where a thin sample is obtained from the volume, the number of required measurements scales with the square of the ratio between the field-of-view and resolution. This is valid even if the 3D nanostructure is characterized on a single slice [72]. For example, a single 2D scanning SAXS measurement with the current scanning parameters of 50 µm step size, 0.03 s per measurement point, and 75 $\times$ 75 points would take 169 seconds, ignoring overhead. If the 3D nanostructure is to be characterized, then 8-10 angles may be measured on the thin sample [72], giving a total of 28 minutes. The same scanning settings for SASTT with the 204 projections applied (see the SI, Table S1) generates a measurement time of 9.6 hours, ignoring overhead. An overview of the employed experimental parameters and the resulting scan time is given in Table S1.

In SASTT, the dose fractionation theorem [74,75] can be applied, because the data measurements are linear and a conventional tomography reconstruction can be used for each scattering direction [25]. According to this theorem, the total dose that is needed for a full tomogram with the same resolution and statistical significance is the same as that needed to measure a thin 2D slice with a thickness equal to the voxel size. This means that the same signal-to-noise ratio for a given q-range can be obtained for both 2D scanning SAXS and SASTT in the same measurement time, provided that all sources of overhead are strongly reduced. However, the current SASTT measurement time is largely determined by the detector used here, which cannot scan faster than 0.03 s exposure time, and the significant overhead of the scanning and rotation stages. In SASTT a higher X-ray energy is also needed to study the large volume, which often results in performance loss of the source and the instrument. However, with the advent of fourth-generation synchrotron sources [76–78] and concomitant upgrades to undulators, X-ray optics, detectors, and dedicated SASTT instrumentation, the photon flux at high energies and scanning speeds may soon allow for faster scans and thus significant increase in sample throughput. In the meantime, studies will likely benefit from a complementary combination of 2D scanning SAXS and SASTT.

4.4. Clinical relevance of the study

This study was designed to investigate the impact of implant degradation and subsequent bone healing on the bone nanostructure, following previous studies by the authors. We have previously been able to follow the nanostructural rearrangement during progressing bone healing and implant degradation [50] and to characterize the impact of Mg on the bone nanostructure and mineral crystal structure. We also elucidated the bone-physiological response of fast Mg release [21]. However, several factors, such as the fast initial response towards implant placement, a possible out-of-plane wrapping around the implant, and a hypothesized reorientation of the nanostructure during healing, remained unsolved in our previous 2D investigations, and thus needed a 3D study to understand the sequence of orientational and nanostructural response.

Our study helps to understand how the degradation process affects the bone nanostructure in 3D. However, with respect to clinical application the following needs to be considered. (i) Only one sample per time point was measured due to the limited access to synchrotron sources and the long measurement time of up to 24 hours per sample. We mitigated this by selecting representative samples based on CT scans of the explanted bones, excluding animals that showed any signs of abnormal implant degradation, and by ensuring proper implant placement during the initial surgery (see SI, Figure S1). (ii) The chosen Mg implant pin in a transcortical geometry has limited medical relevance, contrary to either an intramedullary nail or a screw. The aim of this study was, however, to study the specific effect of the ZX10 Mg implant, where the pin geometry helped us to reduce any extended geometrical effects and the transcortical placement allowed us to investigate the influence of different loading situations in one sample. We thus conclude that our key finding of altered mineral particle orientation is an important factor that needs to be considered in clinical application.

5. Summary and conclusions

In summary, this study sheds light on the 3D nanoadaptation of rat femural bone triggered by degrading ZX10 Mg implants. The main findings are the development of smaller-sized mineral particles (T-parameter) in the implant degradation region; the existence of a Mg-degradation product layer surrounding the degrading implant; and a sequence of two orientational motifs as a response to the implant placement and implant-degradation process. The first motif visible after 1 month is a pronounced orientation along the implant direction in distinct zones (Fig. 4d) and a wrapping of the nanostructure around the implant (Fig. 3a). Subsequently, a new motif takes over, which reduces the orientation along the implant and increases the wrapping of the bone nanostructure around it. Upon increased implant degradation, a regular nanostructural bone orientation along the main bone axis is observed, although a certain degree of misorientation still persists (Fig. 4c, f).

By using SAXS tensor tomography, we extended the methodological possibilities and provided new insights into bone-mineral restructuring upon implant degradation. In this way, we were able to detect a thin interfacial bone layer around the degrading implant and to follow its orientational re-arrangement in 3D. In future research we aim towards the modelling of the reconstructed 3D reciprocal-space maps, which will open new possibilities for a 3D characterization of the nanostructures.

Declaration of Competing Interest

The authors declare that they have no known competing financial interests or personal relationships that could have appeared to influence the work reported in this paper.

Acknowledgments

Anders Palmquist is acknowledged for valuable discussions concerning the interpretation of the SEM data. The authors also acknowledge the Paul Scherrer Institut (PSI) for the allocation of two experimental sessions, which were carried out at the cSAXS beamline of PSI's Swiss Light Source. We also would like to thank the Partnership for Soft Condensed Matter (PSCM) at the European Synchrotron Radiation Facility (ESRF) for support during the experiment. The authors also acknowledge funding from the Area of Advance Materials Science at Chalmers University of Technology (ML), the Swiss National Science Foundation (SNF Sinergia, Grant No. CRSII5-180367) (JL), the Laura Bassi Center of Expertise BRIC (Bioresorbable Implants for Children, FFG – Austria) (EM, HE, AW), and the Berndorf Privatstiftung, Austria (HL, TG).

Supplementary materials

Supplementary material associated with this article can be found, in the online version, at doi:10.1016/j.actbio.2021.07.060.

References

[1] N. Reznikov, M. Bilton, L. Lari, M.M. Stevens, R. Kröger, Fractal-like hierarchical organization of bone begins at the nanoscale, Science 360 (2018) eaao2189, doi:10.1126/science.aao2189.
[2] N. Reznikov, R. Shahar, S. Weiner, Bone hierarchical structure in three dimensions, Acta Biomater. 10 (2014) 3815–3826, doi:10.1016/j.actbio.2014.05.024.
[3] W.J. Landis, M.J. Song, A. Leith, L. McEwen, B.F. McEwen, Mineral and organic matrix interaction in normally calcifying tendon visualized in three dimensions by high-voltage electron microscopic tomography and graphic image reconstruction, J. Struct. Biol. 110 (1993) 39–54, doi:10.1006/jsbi.1993.1003.
[4] S. Weiner, W. Traub, Organization of hydroxyapatite crystals within collagen fibrils, FEBS Lett. 206 (1986) 262–266, doi:10.1016/0014-5793(86)80993-0.
[5] S. Weiner, H.D. Wagner, The material bone: structure-mechanical function relations, Annu. Rev. Mater. Sci. 28 (1998) 271–298, doi:10.1146/annurev.matsci.28.1.271.
[6] W. Wagermaier, H.S. Gupta, A. Gourrier, O. Paris, P. Roschger, M. Burghammer, C. Riekel, P. Fratzl, Scanning texture analysis of lamellar bone using microbeam synchrotron X-ray radiation, J. Appl. Crystallogr. 40 (2007) 115–120, doi:10.1107/S0021889806044888.
[7] H.-S. Han, S. Loffredo, I. Jun, J. Edwards, Y.-C. Kim, H.-K. Seok, F. Witte, D. Mantovani, S. Glyn-Jones, Current status and outlook on the clinical translation of biodegradable metals, Mater. Today 23 (2019) 57–71, doi:10.1016/j.mattod.2018.05.018.
[8] D. Pappalardo, T. Mathisen, A. Finne-Wistrand, Biocompatibility of resorbable polymers: a historical perspective and framework for the future, Biomacromolecules 20 (2019) 1465–1477, doi:10.1021/acs.biomac.9b00159.
[9] M. Bohner, Bioresorbable ceramics, in: Degradation Rate of Bioresorbable Materials, Elsevier, 2008, pp. 95–114, doi:10.1533/9781845695033.2.95.
[10] J.-W. Lee, H.-S. Han, K.-J. Han, J. Park, H. Jeon, M.-R. Ok, H.-K. Seok, J.-P. Ahn, K.E. Lee, D.-H. Lee, S.-J. Yang, S.-Y. Cho, P.-R. Cha, H. Kwon, T.-H. Nam, J.H.L. Han, H.-J. Rho, K.-S. Lee, Y.-C. Kim, D. Mantovani, Long-term clinical study and multiscale analysis of in vivo biodegradation mechanism of Mg alloy, Proc. Natl. Acad. Sci. USA 113 (2016) 716–721, doi:10.1073/pnas.1518238113.
[11] W. Wang, G. Jia, Q. Wang, H. Huang, X. Li, H. Zeng, W. Ding, F. Witte, C. Zhang, W. Jia, G. Yuan, The in vitro and in vivo biological effects and osteogenic activity of novel biodegradable porous Mg alloy scaffolds, Mater. Des. 189 (2020) 108514, doi:10.1016/j.matdes.2020.108514.
[12] T. Imwinkelried, S. Beck, B. Schaller, Pre-clinical testing of human size magnesium implants in miniature pigs: implant degradation and bone fracture healing at multiple implantation sites, Mater. Sci. Eng.: C 108 (2020) 110389, doi:10.1016/j.msec.2019.110389.
[13] Y.F. Zheng, X.N. Gu, F. Witte, Biodegradable metals, Mater. Sci. Eng.: R: Rep. 77 (2014) 1–34, doi:10.1016/j.mser.2014.01.001.
[14] Z. Li, X. Gu, S. Lou, Y. Zheng, The development of binary Mg–Ca alloys for use as biodegradable materials within bone, Biomaterials 29 (2008) 1329–1344, doi:10.1016/j.biomaterials.2007.12.021.
[15] F.A. Shah, P. Thomsen, A. Palmquist, A review of the impact of implant biomaterials on osteocytes, J. Dent. Res. 97 (2018) 977–986, doi:10.1177/0022034518778033.
[16] P. Fratzl, N. Fratzl-Zelman, K. Klaushofer, G. Vogl, K. Koller, Nucleation and growth of mineral crystals in bone studied by small-angle X-ray scattering, Calcified Tissue Int. 48 (1991) 407–413, doi:10.1007/BF02556454.
[17] P. Fratzl, H.S. Gupta, O. Paris, A. Valenta, P. Roschger, K. Klaushofer, Diffracting "stacks of cards" - some thoughts about small-angle scattering from bone, in: Scattering Methods and the Properties of Polymer Materials, Springer Berlin Heidelberg, Berlin, Heidelberg, 2005, pp. 33–39, doi:10.1007/b107343.
[18] M. Bünger, M. Foss, K. Erlacher, H. Li, X. Zou, B. Langdahl, C. Bünger, H. Birkedal, F. Besenbacher, J. Pedersen, Bone Nanostructure near Titanium and porous Tantalum implants studied by Scanning small angle x-ray scattering, Eur. Cells Mater. 12 (2006) 81–91, doi:10.22203/eCM.v012a10.
[19] R.M. Hoerth, M.R. Katunar, A. Gomez Sanchez, J.C. Orellano, S.M. Ceré, W. Wagermaier, J. Ballarre, A comparative study of zirconium and titanium implants in rat: osseointegration and bone material quality, J. Mater. Sci.: Mater. Med. 25 (2014) 411–422, doi:10.1007/s10856-013-5074-3.
[20] B. Zeller-Plumhoff, C. Malich, D. Krüger, G. Campbell, B. Wiese, S. Galli, A. Wennerberg, R. Willumeit-Römer, D.C.F. Wieland, Analysis of the bone ultrastructure around biodegradable Mg–xGd implants using small angle X-ray scattering and X-ray diffraction, Acta Biomater. 101 (2020) 637–645, doi:10.1016/j.actbio.2019.11.030.
[21] T.A. Grünewald, H. Rennhofer, B. Hesse, M. Burghammer, S.E. Stanzl-Tschegg, M. Cotte, J.F. Löffler, A.M. Weinberg, H.C. Lichtenegger, Magnesium from bioresorbable implants: distribution and impact on the nano- and mineral structure of bone, Biomaterials 76 (2016) 250–260, doi:10.1016/j.biomaterials.2015.10.054.
[22] M. Meischel, D. Hörmann, J. Draxler, E.K. Tschegg, J. Eichler, T. Prohaska, S.E. Stanzl-Tschegg, Bone-implant degradation and mechanical response of bone surrounding Mg-alloy implants, J. Mech. Behav. Biomed. Mater. 71 (2017) 307–313, doi:10.1016/j.jmbbm.2017.03.025.
[23] M.E. Birkbak, H. Leemreize, S. Frølich, S.R. Stock, H. Birkedal, Diffraction scattering computed tomography: a window into the structures of complex nanomaterials, Nanoscale 7 (2015) 18402–18410, doi:10.1039/C5NR04385A.
[24] M. Liebi, M. Georgiadis, A. Menzel, P. Schneider, J. Kohlbrecher, O. Bunk, M. Guizar-Sicairos, Nanostructure surveys of macroscopic specimens by small-angle scattering tensor tomography, Nature 527 (2015) 349–352, doi:10.1038/nature16056.
[25] F. Schaff, M. Bech, P. Zaslansky, C. Jud, M. Liebi, M. Guizar-Sicairos, F. Pfeiffer, Six-dimensional real and reciprocal space small-angle X-ray scattering tomography, Nature 527 (2015) 353–356, doi:10.1038/nature16060.
[26] T.A. Grünewald, M. Liebi, N.K. Wittig, A. Johannes, T. Sikjaer, L. Rejnmark, Z. Gao, M. Rosenthal, M. Guizar-Sicairos, H. Birkedal, M. Burghammer, Mapping the 3D orientation of nanocrystals and nanostructures in human bone: Indications of novel structural features, Sci. Adv. 6 (2020) eaba4171, doi:10.1126/sciadv.aba4171.
[27] C. Aktan, M.B. Ertan, A. Turan, O. Kose, Fixation of small osteochondral fragments in a comminuted distal humerus fracture with magnesium bioabsorbable screws: a case report, Cureus 10 (2018) e3752, doi:10.7759/cureus.3752.
[28] J. Hofstetter, M. Becker, E. Martinelli, A.M. Weinberg, B. Mingler, H. Kilian, S. Pogatscher, P.J. Uggowitzer, J.F. Löffler, High-strength low-alloy (HSLA) Mg–Zn–Ca alloys with excellent biodegradation performance, JOM 66 (2014) 566–572, doi:10.1007/s11837-014-0875-5.
[29] T. Kraus, S.F. Fischeraurer, A.C. Hänzi, P.J. Uggowitzer, J.F. Löffler, A.M. Weinberg, Magnesium alloys for temporary implants in osteosynthesis: in vivo studies of their degradation and interaction with bone, Acta Biomater. 8 (2012) 1230–1238, doi:10.1016/j.actbio.2011.11.008.
[30] F. Amerstorfer, S.F. Fischeraurer, L. Fischer, J. Eichler, J. Draxler, A. Zitek, M. Meischel, E. Martinelli, T. Kraus, S. Hann, S.E. Stanzl-Tschegg, P.J. Uggowitzer, J.F. Löffler, A.M. Weinberg, T. Prohaska, Long-term *in vivo* degradation behavior and near-implant distribution of resorbed elements for magnesium alloys WZ21 and ZX50, Acta Biomater. 42 (2016) 440–450, doi:10.1016/j.actbio.2016.06.025.
[31] K. Pichler, T. Kraus, E. Martinelli, P. Sadoghi, G. Musumeci, P.J. Uggowitzer, A.M. Weinberg, Cellular reactions to biodegradable magnesium alloys on human growth plate chondrocytes and osteoblasts, Int. Orthopaed. 38 (2014) 881–889, doi:10.1007/s00264-013-2163-3.
[32] M. Cihova, E. Martinelli, P. Schmutz, A. Myrissa, R. Schäublin, A.M. Weinberg, P.J. Uggowitzer, J.F. Löffler, The role of zinc in the biocorrosion behavior of resorbable Mg–Zn–Ca alloys, Acta Biomater. 100 (2019) 398–414, doi:10.1016/j.actbio.2019.09.021.
[33] S. Jaffari, R.K. Singh Raman, C.H.J. Davies, J. Hofstetter, P.J. Uggowitzer, J.F. Löffler, Stress corrosion cracking and corrosion fatigue characterisation of MgZn1Ca0.3 (ZX10) in a simulated physiological environment, J. Mech. Behav. Biomed. Mater. 65 (2017) 634–643, doi:10.1016/j.jmbbm.2016.09.033.
[34] J. Hofstetter, S. Rüedi, I. Baumgartner, H. Kilian, B. Mingler, E. Povoden-Karadeniz, S. Pogatscher, P.J. Uggowitzer, J.F. Löffler, Processing and microstructure–property relations of high-strength low-alloy (HSLA) Mg–Zn–Ca alloys, Acta Mater. 98 (2015) 423–432, doi:10.1016/j.actamat.2015.07.021.
[35] M. Liebi, M. Georgiadis, J. Kohlbrecher, M. Holler, J. Raabe, I. Usov, A. Menzel, P. Schneider, O. Bunk, M. Guizar-Sicairos, Small-angle X-ray scattering tensor tomography: model of the three-dimensional reciprocal-space map, reconstruction algorithm and angular sampling requirements, Acta Crystallogr. Sect. A Found. Adv. 74 (2018) 12–24, doi:10.1107/S205327331701614X.
[36] P. Kraft, A. Bergamaschi, Ch. Broennimann, R. Dinapoli, E.F. Eikenberry, B. Henrich, I. Johnson, A. Mozzanica, C.M. Schlepütz, P.R. Willmott, B. Schmitt, Performance of single-photon-counting PILATUS detector modules, J Synchrotron Rad. 16 (2009) 368–375, doi:10.1107/S0909049509009911.

[37] C.G. Schroer, M. Kuhlmann, S.V. Roth, R. Gehrke, N. Stribeck, A. Almendarez-Camarillo, B. Lengeler, Mapping the local nanostructure inside a specimen by tomographic small-angle x-ray scattering, Appl. Phys. Lett. 88 (2006) 164102, doi:10.1063/1.2196062.
[38] CXS group, Paul Scherrer Institut, Switzerland, cSAXS matlab package https://www.psi.ch/en/sls/csaxs/software.
[39] S. Pabisch, W. Wagermaier, T. Zander, C. Li, P. Fratzl, Imaging the nanostructure of bone and dentin through small- and wide-angle x-ray scattering, in: Methods in Enzymology, Elsevier, 2013, pp. 391–413, doi:10.1016/B978-0-12-416617-2.00018-7.
[40] P. Bleuet, E. Welcomme, E. Dooryhée, J. Susini, J.-L. Hodeau, P. Walter, Probing the structure of heterogeneous diluted materials by diffraction tomography, Nat. Mater. 7 (2008) 468–472, doi:10.1038/nmat2168.
[41] S.R. Stock, F. De Carlo, J.D. Almer, High energy X-ray scattering tomography applied to bone, J. Struct. Biol. 161 (2008) 144–150, doi:10.1016/j.jsb.2007.10.001.
[42] N.K. Wittig, J. Palle, M. Østergaard, S. Frølich, M.E. Birkbak, K.M. Spiers, J. Garrevoet, H. Birkedal, Bone biomineral properties vary across human osteonal bone, ACS Nano (2019) acsnano.9b05535, doi:10.1021/acsnano.9b05535.
[43] P. Fratzl, M. Groschner, G. Vogl, H. Plenk, J. Eschberger, N. Fratzl-Zelman, K. Koller, K. Klaushofer, Mineral crystals in calcified tissues: a comparative study by SAXS, J. Bone Min. Res. 7 (1992) 329–334, doi:10.1002/jbmr.5650070313.
[44] B. Weinhausen, J.-F. Nolting, C. Olendrowitz, J. Langfahl-Klabes, M. Reynolds, T. Salditt, S. Köster, X-ray nano-diffraction on cytoskeletal networks, New J. Phys. 14 (2012) 085013, doi:10.1088/1367-2630/14/8/085013.
[45] I. Zizak, P. Roschger, O. Paris, B.M. Misof, A. Berzlanovich, S. Bernstorff, H. Amenitsch, K. Klaushofer, P. Fratzl, Characteristics of mineral particles in the human bone/cartilage interface, J. Struct. Biol. 141 (2003) 208–217, doi:10.1016/S1047-8477(02)00635-4.
[46] I. Arganda-Carreras, V. Kaynig, C. Rueden, K.W. Eliceiri, J. Schindelin, A. Cardona, H. Sebastian Seung, Trainable Weka Segmentation: a machine learning tool for microscopy pixel classification, Bioinformatics 33 (2017) 2424–2426, doi:10.1093/bioinformatics/btx180.
[47] N. Sezer, Z. Evis, S.M. Kayhan, A. Tahmasebifar, M. Koç, Review of magnesium-based biomaterials and their applications, J. Magn. Alloys 6 (2018) 23–43, doi:10.1016/j.jma.2018.02.003.
[48] M.P. Staiger, A.M. Pietak, J. Huadmai, G. Dias, Magnesium and its alloys as orthopedic biomaterials: a review, Biomaterials 27 (2006) 1728–1734, doi:10.1016/j.biomaterials.2005.10.003.
[49] R.M. Hoerth, B.M. Seidt, M. Shah, C. Schwarz, B.M. Willie, G.N. Duda, P. Fratzl, W. Wagermaier, Mechanical and structural properties of bone in non-critical and critical healing in rat, Acta Biomater. 10 (2014) 4009–4019, doi:10.1016/j.actbio.2014.06.003.
[50] T.A. Grünewald, A. Ogier, J. Akbarzadeh, M. Meischel, H. Peterlik, S. Stanzl-Tschegg, J.F. Löffler, A.M. Weinberg, H.C. Lichtenegger, Reaction of bone nanostructure to a biodegrading Magnesium WZ21 implant – A scanning small-angle X-ray scattering time study, Acta Biomater. 31 (2016) 448–457, doi:10.1016/j.actbio.2015.11.049.
[51] P. Fratzl, H.S. Gupta, E.P. Paschalis, P. Roschger, Structure and mechanical quality of the collagen–mineral nano-composite in bone, J. Mater. Chem. 14 (2004) 2115–2123, doi:10.1039/B402005G.
[52] R. Baron, R. Tross, A. Vignery, Evidence of sequential remodeling in rat trabecular bone: Morphology, dynamic histomorphometry, and changes during skeletal maturation, Anat. Rec. 208 (1984) 137–145, doi:10.1002/ar.1092080114.
[53] C.L. Li, X.L. Liu, W.X. Cai, W.W. Lu, R.A. Zwahlen, L.W. Zheng, Effect of ovariectomy on stimulating intracortical remodeling in rats, BioMed Res. Int. 2014 (2014) 1–7, doi:10.1155/2014/421431.
[54] F.L. Bach-Gansmo, J.C. Weaver, M.H. Jensen, H. Leemreize, K.S. Mader, M. Stampanoni, A. Brüel, J.S. Thomsen, H. Birkedal, Osteocyte lacunar properties in rat cortical bone: differences between lamellar and central bone, J. Struct. Biol. 191 (2015) 59–67, doi:10.1016/j.jsb.2015.05.005.
[55] V. Ip, Z. Toth, J. Chibnall, S. McBride-Gagyi, Remnant woven bone and calcified cartilage in mouse bone: differences between ages/sex and effects on bone strength, PLoS One 11 (2016) e0166476, doi:10.1371/journal.pone.0166476.
[56] A. Shipov, P. Zaslansky, H. Riesemeier, G. Segev, A. Atkins, R. Shahar, Unremodeled endochondral bone is a major architectural component of the cortical bone of the rat (Rattus norvegicus), J. Struct. Biol. 183 (2013) 132–140, doi:10.1016/j.jsb.2013.04.010.
[57] L.M. Wancket, Animal models for evaluation of bone implants and devices: comparative bone structure and common model uses, Vet. Pathol. 52 (2015) 842–850, doi:10.1177/0300985815593124.
[58] D. Vashishth, O. Verborgt, G. Divine, M.B. Schaffler, D.P. Fyhrie, Decline in osteocyte lacunar density in human cortical bone is associated with accumulation of microcracks with age, Bone 26 (2000) 375–380, doi:10.1016/S8756-3282(00)00236-2.
[59] F.A. Shah, E. Zanghellini, A. Matic, P. Thomsen, A. Palmquist, The orientation of nanoscale apatite platelets in relation to osteoblastic–osteocyte lacunae on trabecular bone surface, Calcif. Tissue Int. 98 (2016) 193–205, doi:10.1007/s00223-015-0072-8.
[60] F. Witte, J. Fischer, J. Nellesen, H.-A. Crostack, V. Kaese, A. Pisch, F. Beckmann, H. Windhagen, In vitro and in vivo corrosion measurements of magnesium alloys, Biomaterials 27 (2006) 1013–1018, doi:10.1016/j.biomaterials.2005.07.037.
[61] F. Witte, J. Fischer, J. Nellesen, C. Vogt, J. Vogt, T. Donath, F. Beckmann, In vivo corrosion and corrosion protection of magnesium alloy LAE442☆, Acta Biomater. 6 (2010) 1792–1799, doi:10.1016/j.actbio.2009.10.012.
[62] Silvia Galli, Jörg U. Hammel, Julia Herzen, Timo Damm, Ryo Jimbo, Felix Beckmann, Ann Wennerberg, Regine Willumeit-Römer, Evaluation of the degradation behavior of resorbable metal implants for in vivo osteosynthesis by synchrotron radiation based x-ray tomography and histology, 2016 in, doi:10.1117/12.2237563.
[63] N. Kawamura, Y. Nakao, R. Ishikawa, D. Tsuchida, M. Iijima, Degradation and biocompatibility of AZ31 magnesium alloy implants in vitro and in vivo: a micro-computed tomography study in rats, Materials 13 (2020) 473, doi:10.3390/ma13020473.
[64] R. Huiskes, H. Weinans, B.V. Rietbergen, The relationship between stress shielding and bone resorption around total hip stems and the effects of flexible materials, Clin. Orthopaed. Relat. Res. (1992) 124–134, doi:10.1097/00003086-199201000-00014.
[65] J. Jeong, J.H. Kim, J.H. Shim, N.S. Hwang, C.Y. Heo, Bioactive calcium phosphate materials and applications in bone regeneration, Biomater. Res. 23 (2019) 4, doi:10.1186/s40824-018-0149-3.
[66] B.W.M. de Wildt, S. Ansari, N.A.J.M. Sommerdijk, K. Ito, A. Akiva, S. Hofmann, From bone regeneration to three-dimensional in vitro models: tissue engineering of organized bone extracellular matrix, Curr. Opin. Biomed. Eng. 10 (2019) 107–115, doi:10.1016/j.cobme.2019.05.005.
[67] A. Matsugaki, N. Fujiwara, T. Nakano, Continuous cyclic stretch induces osteoblast alignment and formation of anisotropic collagen fiber matrix, Acta Biomater. 9 (2013) 7227–7235, doi:10.1016/j.actbio.2013.03.015.
[68] G. Marotti, Osteocyte orientation in human lamellar bone and its relevance to the morphometry of periosteocytic lacunae, Metab. Bone Dis. Relat. Res. 1 (1979) 325–333, doi:10.1016/0221-8747(79)90027-4.
[69] M. Kerschnitzki, W. Wagermaier, P. Roschger, J. Seto, R. Shahar, G.N. Duda, S. Mundlos, P. Fratzl, The organization of the osteocyte network mirrors the extracellular matrix orientation in bone, J. Struct. Biol. 173 (2011) 303–311, doi:10.1016/j.jsb.2010.11.014.
[70] V. Sharma, A. Srinivasan, F. Nikolajeff, S. Kumar, Biomineralization process in hard tissues: the interaction complexity within protein and inorganic counterparts, Acta Biomater. (2020) in press, doi:10.1016/j.actbio.2020.04.049.
[71] S. Kuroshima, M. Yasutake, K. Tsuiki, T. Nakano, T. Sawase, Structural and qualitative bone remodeling around repetitive loaded implants in rabbits: mechanical loading altered bone quality, Clin. Implant Dent. Relat. Res. 17 (2015) e699–e710, doi:10.1111/cid.12318.
[72] M. Georgiadis, M. Guizar-Sicairos, A. Zwahlen, A.J. Trüssel, O. Bunk, R. Müller, P. Schneider, 3D scanning SAXS: a novel method for the assessment of bone ultrastructure orientation, Bone 71 (2015) 42–52, doi:10.1016/j.bone.2014.10.002.
[73] M. Guizar-Sicairos, M. Georgiadis, M. Liebi, Validation study of small-angle X-ray scattering tensor tomography, J. Synchrotron Rad. 27 (2020) 779–787, doi:10.1107/S1600577520003860.
[74] R. Hegerl, W. Hoppe, R. Hegerl, Influence of electron noise on three-dimensional image reconstruction, Z. Naturforschung A 31 (1976) 1717–1721, doi:10.1515/zna-1976-1241.
[75] W. Hoppe, R. Hegerl, W. Hoppe, Some remarks concerning the influence of electron noise on 3D reconstruction, Ultramicroscopy 6 (1981) 205–206, doi:10.1016/S0304-3991(81)80200-8.
[76] P.F. Tavares, E. Al-Dmour, Å. Andersson, F. Cullinan, B.N. Jensen, D. Olsson, D.K. Olsson, M. Sjöström, H. Tarawneh, S. Thorin, A. Vorozhtsov, Commissioning and first-year operational results of the MAX IV 3 GeV ring, J. Synchrotron Radiat. 25 (2018) 1291–1316, doi:10.1107/S1600577518008111.
[77] A. Streun, T. Garvey, L. Rivkin, V. Schlott, T. Schmidt, P. Willmott, A. Wrulich, SLS-2 – the upgrade of the Swiss light source, J. Synchrotron Radiat. 25 (2018) 631–641, doi:10.1107/S1600577518002722.
[78] P. Raimondi, ESRF-EBS: the extremely brilliant source project, Synchrotron Radiat. News 29 (2016) 8–15, doi:10.1080/08940886.2016.1244462.